DOI: 10.3901/CJME.2013.01.104, available online at www.springerlink.com; www.cjmenet.com; www.cjmenet.com.cn

Dynamic Responses of Rotor Drops onto Double-decker Catcher Bearing

ZHU Yili*, JIN Chaowu, and XU Longxiang

College of Mechanical and Electrical Engineering, Nanjing University of Aeronautics and Astronautics, Nanjing 210016, China

Received March 10, 2012; revised July 24, 2012; accepted September 28, 2012

Abstract: In an active magnetic bearing (AMB) system, the catcher bearings (CBs) are indispensable to protect the rotor and stator in case the magnetic bearings fail. Most of the former researches associated with CBs are mainly focused on the dynamic responses of the rotor drops onto traditional single-decker catcher bearings (SDCBs). But because of the lower limited speed of SDCB, it cannot withstand the ultra high speed rotation after rotor drop. In this paper, based on the analysis of the disadvantages of SDCBs, a new type of double-decker catcher bearings (DDCBs) is proposed to enhance the CB work performance in AMB system. In order to obtain the accurate rotor movements before AMB failure, the dynamic characteristics of AMB are theoretically derived. Detailed simulation models containing rigid rotor model, contact model between rotor and inner race, DDCB force model as well as heating model after rotor drop are established. Then, using those established models the dynamic responses of rotor drops onto DDCBs and SDCBs are respectively simulated. The rotor orbits, contact forces, spin speeds of various parts and heat energies after AMB failure are mainly analyzed. The simulation results show that DDCBs can effectively improve the CBs limit rotational speed and reduce the following vibrations, impacts and heating. Finally, rotor drop experiments choosing different types of CBs are carried out on the established AMB test bench. Rotor orbits, inner race temperatures as well as the rotating speeds of both inner race and intermediate races after rotor drop are synchronously measured. The experiment results verify the advantages of DDCB and the correctness of theoretical analysis. The studies provide certain theoretical and experimental references for the application of DDCBs in AMB system.

Key words: active magnetic bearing, dynamic stiffness, rotor drop, double-decker catcher bearing, single-decker catcher bearing, heating

1 Introduction

Active magnetic bearing (AMB) have many advantages over conventional mechanical bearings. In addition to supporting the high-speed rotor without any mechanical friction and lubrication, they enable rotor position and induced vibration to be controlled by adjusting support stiffness and damping. However, catcher bearings (CBs) are necessary to protect the AMB assembly from direct contact with the rotor. They can temporarily support the rotor during maintenance and prevent destruction of the system after a possible AMB failure.

KIRK, et al[1–2], studied the effect of the support stiffness and damping by evaluation of forced response for numerous rotor-support system parameters and showed an optimum damping. SWANSON, et al[3], provided the test results for 38 rotor drops with varying rotor speed, unbalance amplitude and location for the 5 CB configurations. CHEN, et al[4], proposed the zero clearance auxiliary bearing and presented its performance over conventional CB. XIE, et al[5], numerically investigated the steady-stator behavior of a rotor on CB and studied the effects of various parametric configurations: rotor imbalance, support stiffness and damping. COLE, et al[6], developed a deep groove CB model with the elastic deformation of the inner race, which was modeled as a series of flexible beams and studied parametric effects of impact force, bearing width and inner race speed on ball load distributions. However, a rotor drop simulation was not conducted. WANG, et al[7], analyzed the steady-state response of a rigid rotor in a positive clearance bush using the fixed-point algorithm and predicted a chaotic whirling of the rotor depending on excitation frequency.

Most of those researches focused on the rotor dynamic responses after rotor drop. However, as the rotor dynamic characteristics before AMB failure were not detailedly analyzed, the rotor drop simulation results are not reliable. In order to get accurate initial rotor vibration state, the AMB dynamic stiffness serves as the support stiffness before rotor drop is theoretically derived and verified through model experiments.

Rolling element bearings are usually adopted as CBs. Although the optimum catcher bearing stiffness and damping can be obtained from the dynamic simulations, it

---

* Corresponding author. E-mail: nuaazyl@nuaa.edu.cn

This project is supported by National Natural Science Foundation of China (Grant No. 50975134)

is difficult to modify the standard bearing to satisfy the parameter demands. And in most cases the stiffness of traditional catcher bearing turns out to be larger. What is more, once the AMB system fails, the CBs always have to bear extremely high rotating speed that might exceed their limit speed. So a new type double-decker catcher bearing (DDCB) which has two separate rolling element series is proposed in this paper. On one hand, because of the share speed of the intermediate race, the limit speed of this new type CB is improved, so it can withstand higher rotor initial rotating speed. On the other hand, for another bearing is added to the traditional CB, it can to some extent buffer rotor vibrations after rotor drop. According to the actual rotor structure, a rigid rotor dynamic model is build. On the basis of the Hertz contact theory, the collision model between the rotor and inner race is established. Furthermore, a detailed ball bearing model is utilized to gain the real-time support forces after rotor drop. Then the rotor and DDCB dynamic responses and heating are obtained through numerical integration of those dynamic equations. The advantages of the DDCB are verified by both simulation and experiments.

2 AMB Stiffness Analysis

The whole rotor drop process can be divided into two parts: before and after AMB fails. Accurate AMB support stiffness is needed to obtain the initial rotor vibration characteristics. In order to get the AMB dynamic stiffness, firstly, the functional relationship between the control current and vibration displacement should be determined through analyzing AMB system control diagram as shown in Fig. 1.

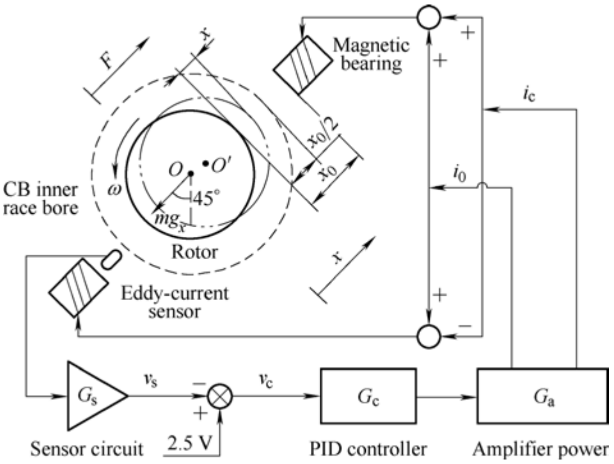

Fig. 1. Control diagram of a 1-DOF AMB system

In the control diagram, i_c is the control current flowing in the coil; v_s is sensor output containing the rotor position information; v_c is input of PID controller, and it is linear with rotor vibration displacement x; x_0 is the balanced air gap, here $x_0 = 0.25$ mm; G_a and G_s are the linear amplifier power gain and sensor gain respectively, here $G_a = 0.4$ A/V and $G_s = 20$ kV/m. According to the control diagram, the relationship between control current and rotor vibration displacement can be expressed as

$$i_c = v_c G_c G_a = (2.5 - v_s) G_c G_a = \\ [2.5 - (0.5x_0 + x)G_s] G_c G_a = -8\,000 x G_c. \tag{1}$$

Before rotor drop the resultant force imposing on the rotor in one direction can be linearized as[8]

$$F = k_x x + k_i i_c, \tag{2}$$

where k_x —Displacement stiffness, $k_x = \mu_0 A N^2 I_0^2 / x_0^3$,
k_i —Current stiffness, $k_i = \mu_0 A N^2 I_0 / x_0^2$.

k_x and k_i can be calculated using the parameters listed in Table 1. The displacement stiffness and current stiffness of each degree are equal because of the complete structure symmetric of the radial magnetic bearings.

Table 1. Parameters of AMB

Parameter	Value
Pole area A/cm^2	1.96
Bias current I_0/A	2
Numbers of the coils N	130
Air magnetic permeability $\mu_0/(\mu\text{H} \cdot \text{m}^{-1})$	0.4π

Substituting Eq. (1), then Eq. (2) becomes

$$F(\mathrm{j}\omega) = -\mathrm{j}8\,000 k_i \,\mathrm{Im}[G_c(\mathrm{j}\omega)] x(\mathrm{j}\omega) + \\ k_x x(\mathrm{j}\omega) - 8\,000 k_i \,\mathrm{Re}[G_c(\mathrm{j}\omega)] x(\mathrm{j}\omega), \tag{3}$$

where ω—Rotor rotational velocity,
$G_c(s)$ —Transfer function of PID controller,

$$G_c(s) = K_p + \frac{K_i}{s} + \frac{K_d s}{1 + \tau_d s},$$

K_p —Proportional coefficient, $K_p = 2.3$,
K_i —Integral coefficient, $K_i = 10$,
K_d —Differential coefficient, $K_d = 1.4 \times 10^{-3}$,
τ_d —Filtering time constant, $\tau_d = 7 \times 10^{-5}$.

The stiffness and damping of AMB can be deduced from Eq. (3):

$$\begin{cases} k = -8\,000 k_i \,\mathrm{Re}[G_c(\mathrm{j}\omega)] + k_x, \\ c = \dfrac{-8\,000 k_i \,\mathrm{Im}[G_c(\mathrm{j}\omega)]}{\omega}. \end{cases} \tag{4}$$

Then the dynamic stiffness of AMB can be expressed as[9–10]

$$k_d = \sqrt{k^2 + (c\omega)^2}. \tag{5}$$

Using the parameters of AMB presented in Table 1, the AMB dynamic stiffness which support the rotor during normal operation can be obtained. Rotor finite element model can be used to calculate the rotor natural frequencies and modal shape using the above-gained dynamic stiffness. The detailed calculation process[11–12] is not list here. The first bend natural frequency is about 800 Hz, which is also verified by model experiments. So the rigid rotor model can be used to analyze the rotor dynamic responses if the rotor spin speed is less than 800 Hz.

3 Dynamic Models

3.1 Rotor model

In order to analyze the rotor dynamic response during the rotor drop process and verify the feasibility and effectiveness of DDCB, the detailed rotor load-carrying model is established in Fig. 2.

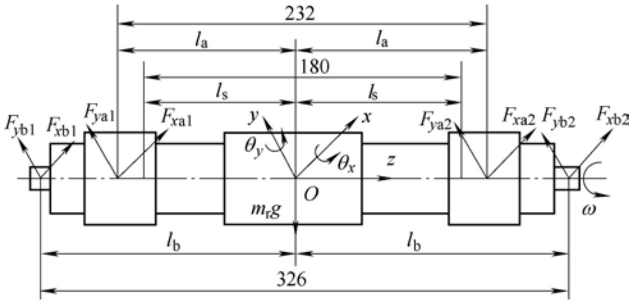

Fig. 2. Rotor structure and load-carrying model (mm)

For the thrust force in the rotor axial direction can be assumed passing through the mass center of the rotor, and the rotor does not exist unbalance in axial direction, the axial subsystem can be separated from the other four radial DOFs[13–14]. Fig. 2 only gives the rotor force analysis in the four radial directions. Where, O is the rotor mass center; x and y denote the axis name; l_a, l_b and l_c are the distances between radial AMB and rotor barycenter, CB and rotor barycenter, radial displacement sensor and rotor barycenter respectively; θ_x and θ_y are the rotor rotary angle in axis x and axis y direction respectively. Each electromagnet force is defined as F_n ($n = x_{aj}$ or y_{aj}, $j = 1, 2$ denote left and right side, respectively); each counterforce from catcher bearing is defined as F_m ($m = x_{bj}$ or y_{bj}). The electromagnetic force can be calculated using the real-time dynamic stiffness. While, detailed collision model between rotor and CB as well as the real-time CB force model should be established to calculate each CB counterforce.

As the rotor works under its first bend natural frequency, rigid rotor model is established to analyze the dynamic responses. According to Fig. 2 the motion formula can be expressed as

$$\boldsymbol{m}\ddot{\boldsymbol{x}} + \boldsymbol{G}\dot{\boldsymbol{x}} = \boldsymbol{A}\boldsymbol{F}_a + \boldsymbol{B}\boldsymbol{F}_b - \boldsymbol{F}_c, \tag{6}$$

where $\boldsymbol{m}$—Rotor mass matrix, $\boldsymbol{m} = \mathrm{diag}(m_r, m_r, J, J)$,

m_r—Rotor mass,

J—Rotor transverse moment of inertia (MOI),

$\boldsymbol{x}$—Displacement vector of rotor barycenter,

$\boldsymbol{x} = (x_o, y_o, \theta_x, \theta_y)^{\mathrm{T}}$,

x_o—Rotor barycenter displacement in x direction,

y_o—Rotor barycenter displacement in y direction,

$\boldsymbol{G}$—Gyro torque matrix,

$$\boldsymbol{G} = \begin{pmatrix} 0 & 0 & 0 & 0 \\ 0 & 0 & 0 & 0 \\ 0 & 0 & 0 & \omega J_z \\ 0 & 0 & -\omega J_z & 0 \end{pmatrix},$$

ω—Rotor rotational speed,

J_z—Polar MOI of the rotor,

$\boldsymbol{A}$, $\boldsymbol{B}$—Introduced parameter matrix,

$$\boldsymbol{A} = \begin{pmatrix} \zeta_{xa1} & 0 & \zeta_{xa2} & 0 \\ 0 & \zeta_{ya1} & 0 & \zeta_{ya2} \\ 0 & l_a & 0 & -l_a \\ -l_a & 0 & l_a & 0 \end{pmatrix},$$

$$\boldsymbol{B} = \begin{pmatrix} 1 & 0 & 1 & 0 \\ 0 & 1 & 0 & 1 \\ 0 & l_b & 0 & -l_b \\ -l_b & 0 & l_b & 0 \end{pmatrix},$$

ζ_{xa1}, ζ_{xa2}, ζ_{ya1}, ζ_{ya2}—Introduced electromagnetic parameters, they equal “1” during normal operation, else equal “0”,

$\boldsymbol{F}_a$, $\boldsymbol{F}_b$, $\boldsymbol{F}_c$—Electromagnetic force, CB counterforce and centrifugal force matrix respectively,

$\boldsymbol{F}_a = (F_{xa1}, F_{ya1}, F_{xa2}, F_{ya2})^{\mathrm{T}}$,

$\boldsymbol{F}_b = (F_{xb1}, F_{yb1}, F_{xb2}, F_{yb2})^{\mathrm{T}}$,

$$\boldsymbol{F}_c = \begin{pmatrix} m_r e_r \omega^2 \cos(\omega t) + m_r g_x \\ m_r e_r \omega^2 \sin(\omega t) + m_r g_y \\ 0 \\ 0 \end{pmatrix},$$

e_r—Rotor unbalance,

g_x—Gravity acceleration in x direction,

g_y—Gravity acceleration in y direction.

The displacement vector $\boldsymbol{x}$ of the rotor barycenter can be expressed using the rotor displacement vector $\boldsymbol{x}_s$ at the two ends of radial sensors:

$$\boldsymbol{x} = \boldsymbol{D}_1 \boldsymbol{x}_s, \tag{7}$$

where $\boldsymbol{x}_s = (x_{s1}, y_{s1}, x_{s2}, y_{s2})^{\mathrm{T}}$,

$\boldsymbol{D}_1$—Displacement transfer matrix,

$$\boldsymbol{D}_1 = \frac{1}{2l_s} \begin{pmatrix} l_s & 0 & l_s & 0 \\ 0 & l_s & 0 & l_s \\ 0 & 1 & 0 & -1 \\ -1 & 0 & 1 & 0 \end{pmatrix}.$$

In the same way, the displacement vector $\boldsymbol{x}_b$ can be derived

$$\boldsymbol{x}_b = \boldsymbol{D}_2^{-1} \boldsymbol{D}_1 \boldsymbol{x}_s, \tag{8}$$

where $\boldsymbol{x}_b = (x_{b1}, y_{b1}, x_{b2}, y_{b2})^{\mathrm{T}}$,

$\boldsymbol{D}_2$—Displacement transfer matrix,

$$\boldsymbol{D}_2 = \frac{1}{2l_\text{b}}\begin{pmatrix} l_\text{b} & 0 & l_\text{b} & 0 \\ 0 & l_\text{b} & 0 & l_\text{b} \\ 0 & 1 & 0 & -1 \\ -1 & 0 & 1 & 0 \end{pmatrix}.$$

By utilizing Eq. (8), the rotor motion Eq. (6) can be rewritten as

$$\boldsymbol{mD}_1\ddot{x}_\text{s} + \boldsymbol{GD}_1\dot{x}_\text{s} = \boldsymbol{AF}_\text{a} + \boldsymbol{BF}_\text{b} - \boldsymbol{F}_\text{c}. \tag{9}$$

Once the AMB system fails, the rotor will drop onto the CBs by gravity. And the rotor speed will be decelerated by the contacts. The rotational equation of motion for the rotor can be given by

$$J_z\ddot{\theta}_\text{r} = (F_\text{t1} + F_\text{t2})R_\text{r}, \tag{10}$$

where F_{tj}—Friction forces between rotor and inner race, and the subscripts rotor mass matrix ($j = 1, 2$), 1, 2 represent the left and right catcher bearing, respectively,

R_r—Radius of the rotor shaft.

3.2 Contact model

In order to improve the rotational speed of the intermediate race, two deep groove ball bearings (61801) are mounted together to constitute the first layer of DDCB, while an outer deep groove ball bearing (61805) act as the second layer that is mounted in the bearing housing. The new type DDCB is the combination of those three bearings. The formed three races are denoted as inner race, intermediate race and outer race, respectively. The detailed structure of DDCB is shown in Fig. 3.

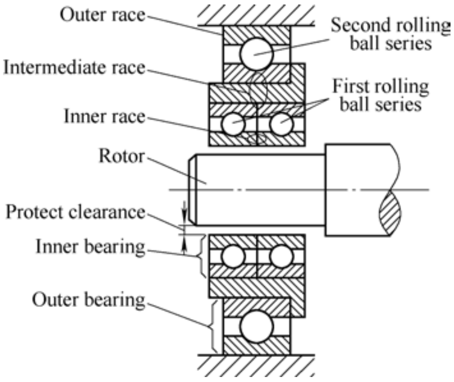

Fig. 3. Structure of DDCB

In order to analyze more simply, it is assumed that there always exit two inner ball and one outer ball vertically below the rotor contact point. Taking the left end for example, the contact model between rotor and inner race as well as DDCB force model are depicted in Fig. 4. Where α_1 is the angle between the direction of the normal contact force and x axis. c_bi1 and c_bo1 are the damping parameters of inner and outer bearings, respectively. Fig. 4 also shows the normal forces acting on the jth inner and kth outer ball, at the angular position φ_{j1} and φ_{k1}, as Q_{ij1} form the inner race, (Q_{oj1}, Q_{ik1}) from the intermediate race and Q_{ok1} from the outer race. T_i1 and T_o1 are the friction torques acting on the inner and outer bearings, respectively. x_bi1 and y_bi1 are the x- and y- displacement of the inner race, and x_bo1 and y_bo1 are the x- and y- displacement of the intermediate race, respectively. $\dot{\theta}_\text{bi1}$ and $\dot{\theta}_\text{bo1}$ separately denote the rotating speed of the inner race and intermediate race.

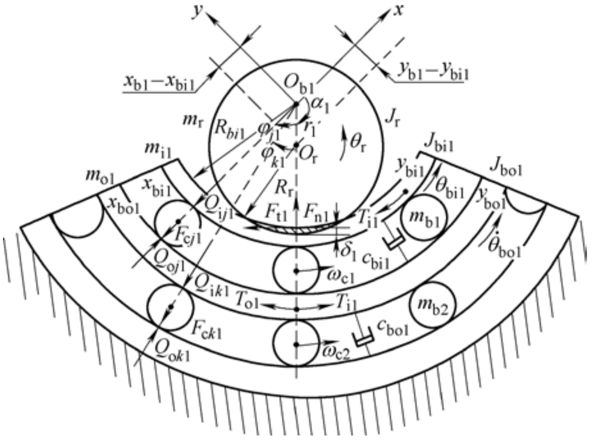

Fig. 4. AMB rotor drop model

A complete contact model includes descriptions of contact force F_n1 and friction force F_t1. A non-linear circle-in-circle contact model can be used to depict the contact between the rotor and the bearing. Based on the Hertz contact theory for two spheres and limited impact velocity below 500 mm/s, the radial contact force F_n1 is a function of the contact penetration δ_1 and the penetration velocity $\dot{\delta}_1$. The radial contact force, which affects the rotor dynamic responses, can be written as follows[15]:

$$F_\text{n1} = \begin{cases} K_\text{c}\delta_1^{10/9}(1 + 0.12\dot{\delta}_1), & \delta_1 > 0, \\ 0, & \delta_1 \leqslant 0, \end{cases} \tag{11}$$

where K_c—Contact stiffness between rotor and inner race,

δ_1—Penetration between the rotor and the inner race, $\delta_1 = r_1 - (R_\text{b1} - R_\text{r})$,

r_1—Radial displacement r_1 between the rotor and the inner race of DDCB with respect to the center of the bearing,

$$r_1 = \sqrt{(x_\text{b1} - x_\text{bi1})^2 + (y_\text{b1} - y_\text{bi1})^2}.$$

The contact stiffness K_c mainly depends on material property and contact geometry: here K_c = 2.4 GN/m. In Eq. (11), the contact forces are avoided by ignoring contact whenever the contact force becomes negative[16].

Using the geometry presented in Fig. 4, the contact angle satisfies:

$$\begin{cases} \sin\alpha_1 = -\dfrac{y_\text{b1} - y_\text{bi1}}{r_1}, \\ \cos\alpha_1 = \dfrac{x_\text{b1} - x_\text{bi1}}{r_1}. \end{cases} \tag{12}$$

And the x- and y- components of the forces applied on the rotor can be calculated as follows:

$$\begin{cases} F_{\mathrm{xb1}} = -F_{\mathrm{n1}} \dfrac{x_{\mathrm{b1}} - x_{\mathrm{bi1}}}{r_1} + F_{\mathrm{t1}} \dfrac{y_{\mathrm{b1}} - y_{\mathrm{bi1}}}{r_1}, \\ F_{\mathrm{yb1}} = -F_{\mathrm{n1}} \dfrac{y_{\mathrm{b1}} - y_{\mathrm{bi1}}}{r_1} - F_{\mathrm{t1}} \dfrac{x_{\mathrm{b1}} - x_{\mathrm{bi1}}}{r_1}. \end{cases} \tag{13}$$

Both slipping and rolling conditions may exist at the contact point. When slipping occurs, the magnitude of the friction force can be calculated as

$$F_{\mathrm{t1}} = \mu_{\mathrm{d}} F_{\mathrm{n1}}, \tag{14}$$

where μ_{d} —Dynamic friction coefficient, $\mu_{\mathrm{d}} = 0.1$.

A rolling condition occurs when the tangential velocity of the inner race reaches the rotor tangential velocity at the contact point. So they satisfy the rolling condition:

$$\dot{\theta}_{\mathrm{r}} R_{\mathrm{r}} = \dot{\theta}_{\mathrm{b1}} R_{\mathrm{b1}}. \tag{15}$$

In this situation, rolling condition Eq. (15), rotor and DDCB dynamic equations should be arranged together to calculate the friction force. Slipping or rolling contacts are determined by the following judgment conditions:

$$\begin{cases} F_{\mathrm{t1}} > \mu_{\mathrm{s}} F_{\mathrm{n1}}, \text{ slip again}, \\ F_{\mathrm{t1}} < \mu_{\mathrm{s}} F_{\mathrm{n1}}, \text{ keep rolling}, \end{cases} \tag{16}$$

where μ_{s} —Maximum static friction coefficient, $\mu_{\mathrm{s}} = 0.2$.

3.3 DDCB model

According to Fig. 4, the dynamic equations DDCB can be written as follows[17]:

$$\boldsymbol{m}_{\mathrm{b1}} \ddot{\boldsymbol{x}}_{\mathrm{b1}} + \boldsymbol{c}_{\mathrm{b1}} \dot{\boldsymbol{x}}_{\mathrm{b1}} = \boldsymbol{F}_{\mathrm{b1}} - \boldsymbol{F}_{\mathrm{br1}}, \tag{17}$$

where $\boldsymbol{m}_{\mathrm{b1}}$—DDCB mass matrix,

$\boldsymbol{m}_{\mathrm{b1}} = \mathrm{diag}(m_{\mathrm{i1}}, m_{\mathrm{i1}}, m_{\mathrm{o1}}, m_{\mathrm{o1}}, J_{\mathrm{bi1}}, J_{\mathrm{bo1}})$,

m_{i1}—Mass of the inner race,

m_{o1}—Mass of the intermediate race,

J_{bi1}—Polar MOI of the inner race,

J_{bo1}—Polar MOI of the intermediate race,

$\boldsymbol{x}_{\mathrm{b1}}$—Displacement vector of the DDCB,

$\boldsymbol{x}_{\mathrm{b1}} = (x_{\mathrm{bi1}}, y_{\mathrm{bi1}}, x_{\mathrm{bo1}}, y_{\mathrm{bo1}}, \theta_{\mathrm{bi1}}, \theta_{\mathrm{bo1}})^{\mathrm{T}}$,

$\boldsymbol{c}_{\mathrm{b1}}$—Damping matrix of the DDCB,

$$\boldsymbol{c}_{\mathrm{b1}} = \begin{pmatrix} 2c_{\mathrm{bi1}} & 0 & -2c_{\mathrm{bi1}} & 0 & 0 & 0 \\ 0 & 2c_{\mathrm{bi1}} & 0 & -2c_{\mathrm{bi1}} & 0 & 0 \\ -2c_{\mathrm{bi1}} & 0 & 2c_{\mathrm{bi1}} + c_{\mathrm{bo1}} & 0 & 0 & 0 \\ 0 & -2c_{\mathrm{bi1}} & 0 & 2c_{\mathrm{bi1}} + c_{\mathrm{bo1}} & 0 & 0 \\ 0 & 0 & 0 & 0 & 0 & 0 \\ 0 & 0 & 0 & 0 & 0 & 0 \end{pmatrix},$$

$\boldsymbol{F}_{\mathrm{b1}}$—External force vector,

$\boldsymbol{F}_{\mathrm{b1}} = (-F_{x\mathrm{b1}}, -F_{y\mathrm{b1}}, 0, 0, F_{\mathrm{t1}} R_{\mathrm{b1}}, 0)^{\mathrm{T}}$,

$\boldsymbol{F}_{\mathrm{br1}}$—Resultant force and moment vector,

$$\boldsymbol{F}_{\mathrm{br1}} = \begin{pmatrix} 2\sum\limits_{j=1}^{Z_{\mathrm{i1}}} Q_{\mathrm{i}j1} \cos(\alpha_1 + \varphi_j) \\ 2\sum\limits_{j=1}^{Z_{\mathrm{i1}}} Q_{\mathrm{i}j1} \sin(\alpha_1 + \varphi_j) \\ \sum\limits_{k=1}^{Z_{\mathrm{o1}}} Q_{\mathrm{i}k1} \cos(\alpha_1 + \varphi_k) - 2\sum\limits_{j=1}^{Z_{\mathrm{i1}}} Q_{\mathrm{o}j1} \cos(\alpha_1 + \varphi_j) \\ \sum\limits_{k=1}^{Z_{\mathrm{o1}}} Q_{\mathrm{i}k1} \sin(\alpha_1 + \varphi_k) - 2\sum\limits_{j=1}^{Z_{\mathrm{i1}}} Q_{\mathrm{o}j1} \sin(\alpha_1 + \varphi_j) \\ -2T_{\mathrm{i1}} \\ 2T_{\mathrm{i1}} - T_{\mathrm{o1}} \end{pmatrix}.$$

The contact force at the ball-race interfaces can be calculated using Hertz contact theory[18]. Assuming the races are rigid, the elastic deformation of the inner and outer balls due to local contact stresses can be calculated as

$$\begin{pmatrix} \sigma_{j1} \\ \sigma_{k1} \end{pmatrix} = \begin{pmatrix} \left(\dfrac{Q_{\mathrm{i}j1}}{k_{\mathrm{i}j1}}\right)^{2/3} + \left(\dfrac{Q_{\mathrm{o}j1}}{k_{\mathrm{o}j1}}\right)^{2/3} \\ \left(\dfrac{Q_{\mathrm{i}k1}}{k_{\mathrm{i}k1}}\right)^{2/3} + \left(\dfrac{Q_{\mathrm{o}k1}}{k_{\mathrm{o}k1}}\right)^{2/3} \end{pmatrix}, \tag{18}$$

where $k_{\mathrm{i}j1}$, $k_{\mathrm{o}j1}$—Contact stiffness parameters between the inner ball and corresponding races,

$k_{\mathrm{i}k1}$, $k_{\mathrm{o}k1}$—Contact stiffness parameters between the outer ball and corresponding races.

Those stiffness parameters can be calculated using the given DDCB material and geometrical parameters, as shown in Table 2. The detailed description of the calculation process can be found in Ref. [18].

From Fig. 4 according to the geometric relationships the elastic deformation can also be represented by

$$\begin{pmatrix} \sigma_{j1} \\ \sigma_{k1} \end{pmatrix} = \begin{pmatrix} (x_{\mathrm{bi1}} - x_{\mathrm{bo1}}) \cos(\alpha_1 + \varphi_{j1}) + \\ (y_{\mathrm{bi1}} - y_{\mathrm{bo1}}) \sin(\alpha_1 + \varphi_{j1}) - c_{\mathrm{ri}} \\ x_{\mathrm{bo1}} \cos(\alpha_1 + \varphi_{k1}) + y_{\mathrm{bo1}} \sin(\alpha_1 + \varphi_{k1}) - c_{\mathrm{ro}} \end{pmatrix}, \tag{19}$$

where c_{ri}—Diametric clearance of the inner bearings,

c_{ro}—Diametric clearance of the outer bearings.

By arranging Eqs. (18) and (19), those contact forces can be expressed using the calculated contact stiffness parameters and the geometrical parameters. The ball load equilibrium equations including the centrifugal force are derived as

$$\begin{pmatrix} Q_{\mathrm{o}j1} \\ Q_{\mathrm{o}k1} \end{pmatrix} = \begin{pmatrix} Q_{\mathrm{i}j1} + F_{\mathrm{c}j1} \\ Q_{\mathrm{i}k1} + F_{\mathrm{c}k1} \end{pmatrix} = \begin{pmatrix} Q_{\mathrm{i}j1} + \dfrac{d_{\mathrm{pi}} m_{\mathrm{bi}} \omega_{\mathrm{ci}}^2}{2} \\ Q_{\mathrm{i}k1} + \dfrac{d_{\mathrm{po}} m_{\mathrm{bo}} \omega_{\mathrm{co}}^2}{2} \end{pmatrix}, \tag{20}$$

where d_{pi}, d_{po}—Pitch diameters of the inner and outer bearing respectively,

m_{bi}, m_{bo}—Ball masses of the inner and outer bearing respectively,

ω_{ci}, ω_{co}—Cage revolution speeds of the inner and outer bearing respectively,

$$\begin{pmatrix}\omega_{\mathrm{ci}}\\ \omega_{\mathrm{co}}\end{pmatrix}=\begin{pmatrix}\dfrac{\dot{\theta}_{\mathrm{bi1}}(d_{\mathrm{pi}}-d_{\mathrm{bi}})+\dot{\theta}_{\mathrm{bo1}}(d_{\mathrm{pi}}+d_{\mathrm{bi}})}{2d_{\mathrm{pi}}}\\ \dfrac{\dot{\theta}_{\mathrm{bo1}}(d_{\mathrm{po}}-d_{\mathrm{bo}})}{2d_{\mathrm{po}}}\end{pmatrix},$$

d_{bi}, d_{bo}—Ball diameters of the inner and outer bearing respectively.

Table 2. Specification of rotor drop simulation parameters

Rotor parameter	
Parameter	**Value**
Imbalance eccentricity e_{r}/mm	0.008
Gravity acceleration in x direction g_x/(m • s^{-2})	6.93
Gravity acceleration in y direction g_y/(m • s^{-2})	6.93
Polar MOI J_z/(kg • mm^2)	380
Transverse MOI J/(kg • mm^2)	1.6×10^4
Distance between AMB and rotor barycenter L_a/m	0.116
Distance between CB and rotor barycenter L_b/m	0.163
Distance between radial sensor and rotor barycenter L_c/m	0.09
Mass m_{r}/kg	2.14
Journal radius R_{r}/mm	5.875

DDCB parameter	
Parameter	**Value**
Static load rating of inner bearing C_{si1}/kN	1.9
Static load rating of outer bearing C_{so1}/kN	4.3
Damping coefficient of the inner bearing c_{bi1}/(N • s • m^{-1})	250
Damping coefficient of the outer bearing c_{bo1}/(N • s • m^{-1})	500
Diametric clearance of the inner bearing c_{ri}/μm	6
Diametric clearance of the outer bearing c_{ro}/μm	10
Diameter of inner ball d_{bi}/mm	2.381
Diameter of outer ball d_{bo}/mm	3.5
Pitch diameter of inner bearing d_{pi}/mm	16.5
Pitch diameter of outer bearing d_{po}/mm	31
Elastic modulus of ball E_{b}/GPa	290
Elastic modulus of races E_{r}/GPa	208
Polar MOI of inner race	0.16
Polar MOI of intermediate race	4.19
Mass of inner ball m_{bi}/mg	55
Mass of outer ball m_{bo}/g	0.18
Mass of inner race m_{i1}/g	3.6
Mass of intermediate race m_{o1}/g	28
Bore radius R_{bi1}/mm	6
Number of the inner balls z_{i1}	12
Number of the outer balls z_{o1}	15
Poisson ratio of ball v_{b}	0.26
Poisson ratio of races v_{r}	0.3
Viscosity $\nu_{\mathrm{i1,o1}}$/(mm^2 • s^{-1})	25
Density of ball and races: steel ρ/(g • cm^{-2})	7.8

The internal friction torque acting on the left DDCB can be written using Palmgren's theory[19]:

$$\begin{pmatrix}T_{\mathrm{i1}}\\ T_{\mathrm{o1}}\end{pmatrix}=\begin{pmatrix}T_{\mathrm{li1}}+T_{\mathrm{vi1}}\\ T_{\mathrm{lo1}}+T_{\mathrm{vo1}}\end{pmatrix}, \tag{21}$$

where T_{li1}, T_{lo1}—Load-dependent friction torques of inner and outer bearing respectively,

$$\begin{pmatrix}T_{\mathrm{li1}}\\ T_{\mathrm{lo1}}\end{pmatrix}=\begin{pmatrix}\dfrac{f_1 d_{\mathrm{p1}}F_{\mathrm{n1}}}{2}\left(\dfrac{F_{\mathrm{n1}}}{2C_{\mathrm{si1}}}\right)^{0.55}\\ f_2 d_{\mathrm{p2}}F_{\mathrm{n1}}\left(\dfrac{F_{\mathrm{n1}}}{C_{\mathrm{so1}}}\right)^{0.55}\end{pmatrix},$$

C_{si1}, C_{so1}—Static load rating of the inner and outer bearing respectively,

f_1, f_2—Factors that vary from 0.000 2 to 0.000 4, $f_1=f_2=0.000\,3$,

T_{vi1}, T_{vo1}—Viscous friction torques of inner and outer bearing respectively,

$$\begin{pmatrix}T_{\mathrm{vi1}}\\ T_{\mathrm{vo1}}\end{pmatrix}=\begin{pmatrix}10^{-7}\varsigma_{11}(\nu_{\mathrm{i1}}n_{\mathrm{i1}})^{2/3}d_{\mathrm{p1}}^3+160\times10^{-7}\varsigma_{21}f_{\mathrm{i1}}d_{\mathrm{p1}}^3\\ 10^{-7}\varsigma_{12}(\nu_{\mathrm{o1}}n_{\mathrm{o1}})^{2/3}d_{\mathrm{p2}}^3+160\times10^{-7}\varsigma_{22}f_{\mathrm{o1}}d_{\mathrm{p2}}^3\end{pmatrix},$$

$f_{\mathrm{i1}}, f_{\mathrm{o1}}$—Factors depending on the bearing type and the method of lubrication,

$\nu_{\mathrm{i1}}, \nu_{\mathrm{o1}}$—Kinematic viscosity of the lubricant in centistrokes for the inner and outer bearing, respectively,

n_{i1}—Inner bearing work speed, $n_{\mathrm{i1}}=30(\dot{\theta}_{\mathrm{bi1}}-\dot{\theta}_{\mathrm{bo1}})/\pi$,

n_{o1}—Outer bearing work speed, $n_{\mathrm{o1}}=30\dot{\theta}_{\mathrm{bo1}}/\pi$,

ς_{ab}—Introduced parameters, $a=1, 2$; $b=1, 2$.

In practice, the values for deep groove ball bearings range between 0.7 and 2. In this study, the parameters $f_{\mathrm{i1,o1}}$ are selected to be 1. If $v_{\mathrm{ob}}n_{\mathrm{b}}\leqslant 2\,000$, $\varsigma_{1b}=0$, $\varsigma_{1b}=1$; else $\varsigma_{1b}=1$, $\varsigma_{1b}=0$.

3.4 Heating model

Heating after rotor drop is another major problem, for excessive heating may damage CBs that directly influences the safety of the whole system. A CB has a variety of heat sources, and here two major sources are considered during the rotor drop: rotor/CB mechanical rub and drag torque. When adopting DDCB, the thermal power loss in the left end is

$$H_1=\frac{1}{2}H_{\mathrm{r1}}+H_{\mathrm{b1}}, \tag{22}$$

where H_{r1}—Power loss generated by rotor and CB mechanical rub,

$$H_{\mathrm{r1}}=F_{\mathrm{t1}}(R_{\mathrm{r}}\dot{\theta}_{\mathrm{r}}-R_{\mathrm{bi1}}\dot{\theta}_{\mathrm{bi1}})+F_{\mathrm{t1}}[(\dot{x}_{\mathrm{bi1}}-\dot{x}_{\mathrm{b1}})\sin\alpha_1+(\dot{y}_{\mathrm{b1}}-\dot{y}_{\mathrm{bi1}})\cos\alpha_1],$$

H_{r1}—Power loss caused by the CB,

$$H_{\mathrm{b1}}=2T_{\mathrm{i1}}(\dot{\theta}_{\mathrm{bi1}}-\dot{\theta}_{\mathrm{bo1}})+T_{\mathrm{o1}}\dot{\theta}_{\mathrm{bo1}}.$$

While for SDCB $H_{\mathrm{b1}}=2T_{\mathrm{i1}}\dot{\theta}_{\mathrm{bi1}}$. The corresponding total heat energy can be obtained by integrating the thermal power loss:

$$E_1=E_{\mathrm{r1}}+E_{\mathrm{b1}}=\frac{1}{2}\int_0^t H_{\mathrm{r1}}(t)\mathrm{d}t+\int_0^t H_{\mathrm{b1}}(t)\mathrm{d}t, \tag{23}$$

where E_{r1} —Heat energy generated by rotor and CB mechanical rub,

E_{b1} —Heat energy caused by the CB.

4 Simulation Results

In this section, using a variable time-step fourth order Runge-Kutta[20] integration algorithm, both of the numerical solutions after rotor drop in AMB system choosing DDCBs and traditional SDCBs respectively are obtained to identify the different dynamic responses of these two various CB types. As the inner bearings of DDCB are the same type of SDCB, for simplicity the elastic deformation of the outer balls can be assumed to be zero to calculate the rotor responses when rotor drops onto SDCBs. The detailed parameters are listed in Table 2.

Firstly, rotor vibration displacements and velocities in *X*- and *Y*- directions are obtained through solving Eq. (20) for normal operation. After the initial transient motion has damped out, the rotor motion turns out to be the circular synchronous precession. When the barycenter of rotor crosses the vertical axis at the lower point, the AMBs' power is assumed to be cut off: here the introduced parameters ζ_{xa1}, ζ_{xa2}, ζ_{ya1}, and ζ_{ya2} equal "0". Then, by utilizing the rotor motion conditions of this point, Eqs. (9)–(10) and (17) are solved for rotor drop. In the simulation program, a very small boundary (1×10^{-6}) is added around zero to judge the relative velocity between the rotor and inner race. And if the relative velocity is within this boundary, the rolling condition is applied to determine the tangential contact forces, otherwise, a slipping condition is applied.

Figs. 5(a)–5(b) show simulation orbits of the left journal for different CB types from 0 to 0.2 s after rotor drop. The nominal catcher bearing clearance circle is also shown with the orbit plots. It can be seen from the figure that, the angular range of the rotor vibration using DDCBs is about 120° which is significantly smaller than the range (270°) using SDCBs. And the use of DDCBs helps to decrease the amplitudes of rotor vibration about 30% after rotor drop.

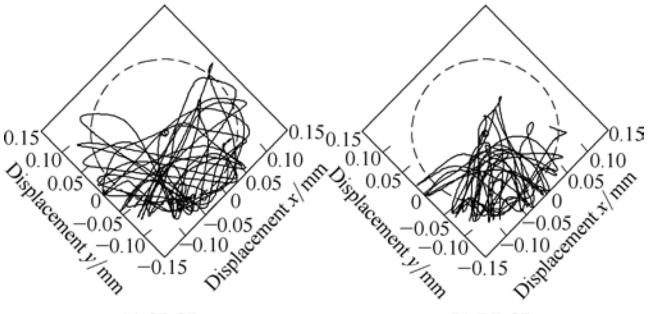

(a) SDCB　　(b) DDCB

Fig. 5. Orbits of the left journal obtained by simulations for various CB types

The contact forces between the left journal and inner race after rotor drop are presented in Fig. 6. Due to the added outer rolling bearing, the support stiffness of the DDCB is smaller, while the damping is larger. The changes of the support characteristics make the maximum contact forces drop about 20%–30% compared to the initial results using SDCBs. Because of the increase of the support damping, the contact force using DDCBs decays a little faster.

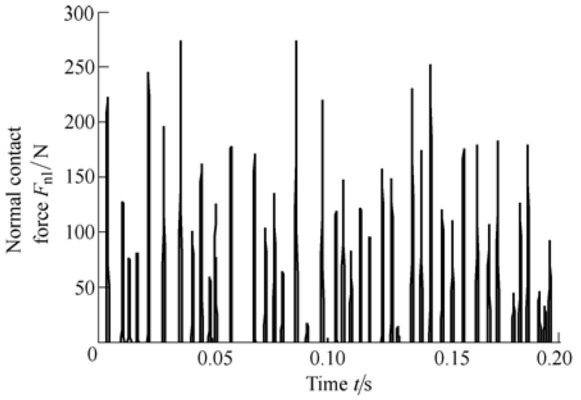

(a) SDCB

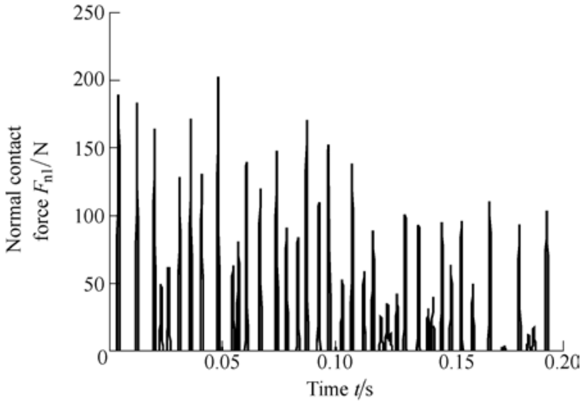

(b) DDCB

Fig. 6. Contact forces between the left journal and inner race obtained by simulations for various CB types

To gain a better understanding of the dynamical behavior of DDCB, the revolutions of the rotor, inner race and intermediate race from 0 to 0.5 s after rotor drop with the initial rotor speed 200 Hz are shown in Fig. 7.

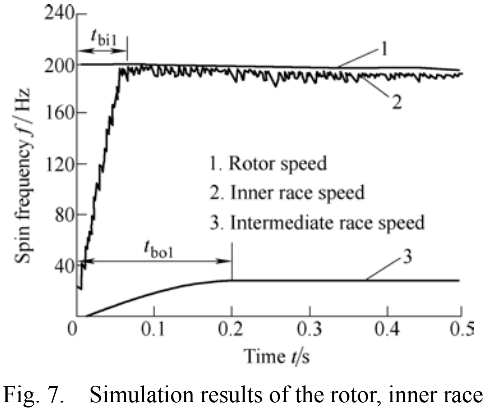

Fig. 7. Simulation results of the rotor, inner race and intermediate race rotational frequencies

The inner race is accelerated very quickly up to the maximum velocity. At the time $t_{bi1}\approx0.06$ s, inner race and rotor have the same tangential velocity, but different rotational frequencies for the various radiuses. After the time t_{bi1} the inner race continues acceleration and deceleration process but has relatively smaller speed fluctuations. The acceleration time of the intermediate race t_{bo1} is a little longer than t_{bi1} because of the smaller drive torque and larger polar MOI. After the time $t_{\mathrm{bo1}}\approx0.2$ s the spin speed of intermediate race has very small fluctuation and keeps about 17% of the inner race speed. And the rotor spin speed keep reducing during the presented time, because a part of the rotor energy is transferred to heat and DDCBs kinetic energy.

The heat produced by the mechanical rub between rotor and inner race after rotor drop can be calculated after the dynamic simulation, as shown in Fig. 8. It can be seen that the generated heat energy in DDCB at 0.2 s after rotor drop is about 25% less than the energy using SDCB. Two main reasons cause this result: the smaller support stiffness and larger damping of DDCBs leads to relatively smaller tangential friction force. Furthermore, the rotating of the intermediate race to some extent reduces the tangential relative velocity between the rotor and inner race at the contact point. During the inner race acceleration process, the heat energy rises quite quickly because there is relative motion between the rotor and the inner race. After the inner race speed almost equals to the rotor speed, the heat energy rises very slowly for the little heat produced by sliding.

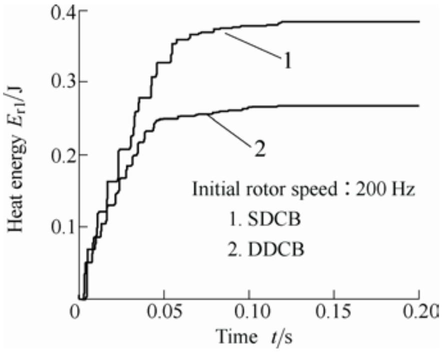

Fig. 8. Heat energy caused by rotor/CB mechanical rub in the left CB obtained by simulations for various CB types

5 Experiment Results

Rotor drop experiments for different CB types are carried out to verify the established dynamic models and the performance of DDCB. Fig. 9 shows the mechanical parts of DDCB, SDCB as well as the corresponding bearing blocks.

Fig. 10 shows the experimental facilities necessary for measurement. The system adopts eddy current sensor to realize the measurement of rotor vibration displacement, which also have to be known for controlling the AMBs anyway. A fiber sensor is used to detect the black and white stripes painted on the rotor. Then the rotor spin velocity can be calculated by using the output signal of the fiber sensor collected by the Labview data acquisition (DAQ). In order to quantify the rotating speeds of the inner and intermediate races, two fiber sensors are adopted. The measurement principle is the same as that for the rotor spin velocity. Infrared thermo scope is used to measure the CB's real-time temperature after rotor drop. The data acquisition boards collect all the sensor signals except the temperature signals. For the data acquisition, three boards NI-9215 from National Instruments are chosen. A subsequent analysis of the collected data is carried out with MATLAB software.

Fig. 9. Photograph of the CBs and CB blocks

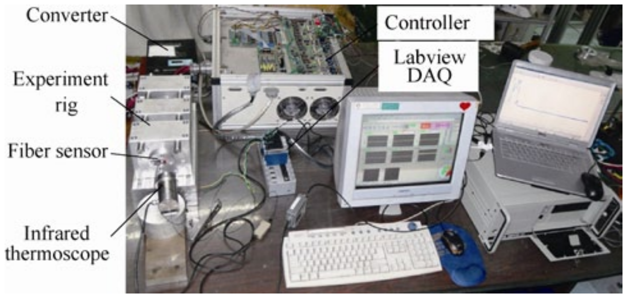

Fig. 10. Photograph of the Experimental facilities

Figs. 11(a)–11(b) present the experiment orbits of the left journal after rotor drop at the rotor initial rotating frequency 200 Hz. In this experiment we observe that the vibration limits using DDCBs are relatively smaller. Comparing Fig. 5 and Fig. 11, the experimental results are correspondent with the simulation results, which also verify the correctness of the established dynamic models.

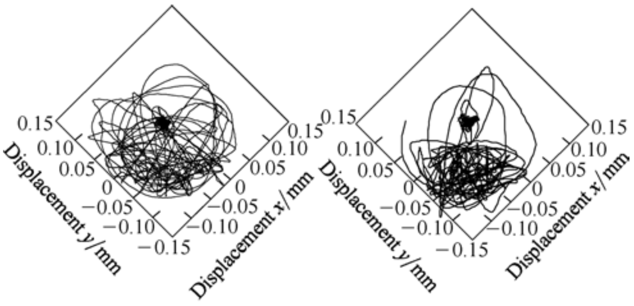

(a) SDCB (b) DDCB

Fig. 11. Orbits of the left journal obtained by experiments

The measured rotational frequencies of different rotating parts after rotor drop are shown in Fig. 12. The acceleration time $t_{\text{bi1}}\approx0.04$ s and $t_{\text{bo1}}\approx0.15$ s are shorter than the simulation results. We can conclude that the practical contact and friction forces might be a little larger. What is more, the rotor speed decline and the speed fluctuation of the both inner and intermediate race are larger than simulation results. Except for the external forces, other factors such as the bearing internal sliding, machining and assembly errors, disturbing signals, and so on, can also lead to the larger fluctuation. But analyzing the speed ratio of the two races and the entire tendency, the calculation results show good agreement with the experimental measurements.

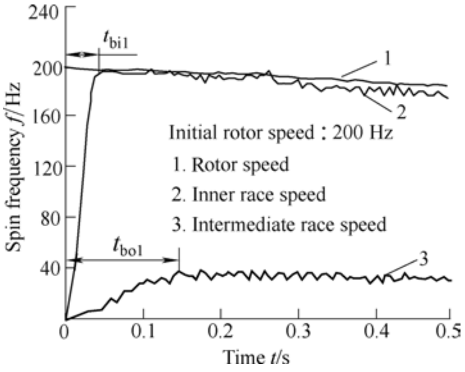

Fig. 12. Experiment results of the rotor, inner race and intermediate race spin frequencies

The measured temperature rises of the CB inner races after rotor drop are presented in Fig. 13. The maximum temperature rises of the DDCB inner race are about 50% of that of the SDCB inner race. Comparing Fig. 8 and Fig. 13, because of the heat transfer process, the temperature rise relative to heat energy rise has certain hysteresis. The experiment results also verify the effect of DDCBs on reducing the following temperature rise after rotor drop.

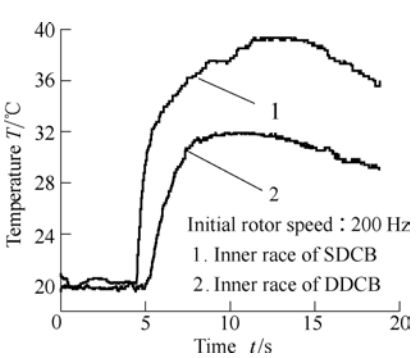

Fig. 13. Temperature rises of various CB types after rotor drop

6 Conclusions

(1) Use of DDCBs makes the rotor vibration amplitudes after rotor drop decrease about 30%.

(2) The maximum contact force between journal and inner race reduces about 20%–30% when adopting DDCBs, what is more, the decay rate of the contact forces is faster.

(3) The angular acceleration of the intermediate race is a little smaller than that of the inner race. After the acceleration time, the speed of the intermediate race keeps about 17% of the rotating inner race speed.

(4) The heat energy generated in the left DDCB at 0.2s after rotor drop is only about 75% of the energy when using SDCBs. Furthermore, the measured maximum DDCB temperature rise after rotor drop is only about 50% of the SDCB temperature rise.

In a word, except for the higher limit speed, taking the rotor vibration amplitudes, contact forces and heating after rotor drop in view, DDCBs are more suitable for CBs used in AMB system.

References

[1] ISHII T, KIRK R G. Transient response technique applied to active magnetic bearing machinery during rotor drop[J]. *Journal of Vibration and Acoustics*, 1996, 2: 154–164.

[2] KIRK R G, ISHII T. Transient rotor drop analysis of rotor following magnetic bearing power outage[C]//*Proceedings of MAG '93 Magnetic Bearings, Magnetic Drives, and Dry Gas Seals Conference & Exhibition*, Alexandria, VA, USA, 1993: 53–61.

[3] KIRK R G, SWANSON E E, KAVARANA F H, et al. Rotor drop test stand for AMB rotating machinery—part I: description of test stand and initial results[C]//*Proceedings of the Fourth International Symposium on Magnetic Bearings*, Zurich, Switzerland, 1994: 207–212.

[4] CHEN H M, WALTON J, HESHMAT H. Test of a zero clearance auxiliary bearing[C]//*Proceedings of MAG '97 Industrial Conference and Exhibition on Magnetic Bearings*, Alexandria, VA, USA, 1997: 111–119.

[5] XIE H, FLOWERS T. Steady-state dynamic behavior of an auxiliary bearing supported rotor system[C]//*American Society of Mechanical Engineers Winter Annual Meeting*, Chicago, USA, 1994: 1–11.

[6] COLE M O T, KEOGH P S, BURROWS C R. The dynamic behavior of a rolling element auxiliary bearing following rotor impact[J]. *Journal of Tribology*, 2002, 124: 406–613.

[7] WANG X, NOAH S. Nonlinear dynamics of a magnetically supported rotor on safety auxiliary bearings[J]. *Journal of Vibration and Acoustics*, 1998, 120: 596–606.

[8] POLAJZER B, STUMBERGER G, RITONJA J, et al. Variations of active magnetic bearings linearized model parameters analyzed by finite element computation[J]. *IEEE Transactions on Magnetics*, 2008, 44(6): 1 534–1 537.

[9] SUN Yanhua, HO Y S, YU Lie. Dynamic stiffnesses of active magnetic thrust bearing including eddy-current effects[J]. *IEEE Transactions on Magnetics*, 2009, 45(1): 139–149.

[10] ZHAO Lei, CONG Hua, ZHAO Hongbin. Study on stiffness and damping characteristic of active magnetic bearing[J]. *Journal of Tsinghua University*, 1999, 39(4): 96–99.

[11] MONTIEL M A, NAVARRO G S. Finite element modeling and unbalance compensation for a two disks asymmetrical rotor system[C]//*Fifth International Conference on Electrical Engineering, Computing Science and Automatic Control*, Mexico City, Mexico, November, 2008: 386–391.

[12] GU Jialiu. *Rotor dynamics*[M]. Beijing: National Defense Industrial Press, 1985.

[13] HIJIKATA K, TAKEMOTO M, OGASAWARA S, et al. Behavior of a novel thrust magnetic bearing with a cylindrical rotor on high speed rotation[J]. *IEEE Transactions on Magnetics*, 2009, 45(10): 4 617–4 620.

[14] KHOO K S, KALITA K, GARVEY S D, et al. Active axial-magnetomotive force parallel-airgap serial flux magnetic bearings[J]. *IEEE Transactions on Magnetics*, 2010, 46(7): 2 596–2 602.

[15] SUN G, PALAZZOLO A, PROVENZA A, et al. Detailed ball bearing model for magnetic suspension auxiliary service[J]. *Journal of Sound and Vibration*, 2004, 269: 933–963.

[16] MARKERT R, WEGENER G. Transient vibration of elastic rotors in retainer bearings[C]//*Proceedings of the Seventh International Symposium on Transport Phenomena and Dynamics of Rotating Machinery,* Honolulu, USA, 1998: 764–774.

[17] HU Haiyan, SUN Jiuhou, CHEN Huaihai. *Mechanical vibration and shock*[M]. Beijing: Aviation Industry Press, 1998.

[18] HARRIS. *Rolling bearing analysis*[M]. 4th ed. New York: John Wiley & Sons, Inc., 2001.

[19] Gang Ben Chun San (Japanese). *Design and calculation of ball bearing*[M]. Beijing: China Machine Press, 2004.

[20] HAIRER E, NORSETT S P, WANNER G. *Solving ordinary differential equations I: non-stiff problem*[M]. New York: Springer, 1993.

Biographical notes

ZHU Yili received his BSc degree from *College of Mechanical and Electrical Engineering, Nanjing University of Aeronautics and Astronautics, China*, in 2007. Currently, he is a PhD candidate.
Tel: +86-25-84892594; E-mail: nuaazyl@nuaa.edu.cn

JIN Chaowu received his Master degree from *College of Mechanical and Electrical Engineering, Nanjing University of Aeronautics and Astronautics, China*, in 2006. Currently, he is a PhD candidate.
E-mail: jinchaowu@nuaa.edu.cn

XU Longxiang received his BSc degree from *Zhejiang University, China*, in 1983. In 1990, he received his PhD degree in mechanics from *Xi'an Jiaotong University, China.* From March 1990 to now, he worked at *College of Mechanical and Electrical Engineering, Nanjing University of Aeronautics and Astronautics, China*. From April 1998 to April 1999, he was a senior visiting scholar at *International Center for Magnetic Bearings, Swiss Federal Institute of Technology*. From April 1999 to December 1999, he also worked at *International Center for Magnetic Bearings, Swiss Federal Institute of Technology*. His main research fields include magnetic levitating bearing, rotor dynamics, mechanical design, the bearingless motors, and Maglev fan.
E-mail: fqp@nuaa.edu.cn